ADVANCED FUNCTIONAL MATERIALS
www.afm-journal.de



# High Contrast Superlens Lithography Engineered by Loss Reduction

*Hong Liu, Bing Wang, Lin Ke, Jie Deng, Chan Chum Choy, Ming Sheng Zhang, Lu Shen, Stefan A. Maier,* and Jing Hua Teng**

**Although sub-diffraction-limit-resolution optical imaging has been attained via superlenses in the UV regime, the corresponding resist profile in general exhibits a very poor contrast, far below the minimum requirement for photolithography. Here, it is experimentally demonstrated thin flat silver superlenses, engineered through refining interfacial roughness to reduce scattering loss, capable of resolving grating features of sub-50 nm resolution with a high contrast of about 2.2. The seed layer effect on the superlens performance at a wavelength of 365 nm has been probed through both experimental and analytical methods. The performance of Ag, Ag/Ni and Ag/Ge superlenses agrees well with theoretical predications. The results show that a smooth interface is a key factor for realizing high performance superlensing, while damping losses become dominant when the roughness is reduced to less than 2 nm. This work verifies that a superlens is a potential tool for sub-diffraction limit nano-photolithography.**

## 1. Introduction

The superlens concept, since its first conceptualization on 2000,[1] has attracted tremendous interest and intensive studies for its capability of beating the diffraction limit in imaging. A superlens employs a thin metallic layer of a negative dielectric permittivity to generate surface plasmons (SPs) so as to restore the high wave-vector components encoded in evanescent waves, which carry the fine feature information of the near field. In contrast, a conventional optical lens made of positive-index materials is only able to resolve objects on the order of half-wavelength separation via propagating waves, which makes it suffer from the diffraction limit. Experimental demonstrations of sub-diffraction-limit imaging by a superlens have been achieved in the microwave,[2–4] optical frequency[5–9] and mid-infrared regime[10] in succession. Superlens lithography (SL) in the UV regime has also been envisioned as a potential technique for high throughput nano-patterning.[11] In fact in the past decade, not only SL, but also other SPs-based lithographic approaches have been extensively studied and been categorized as an emerging technology termed as plasmonic lithography (PL). PL is a novel and attractive technique to devote SPs to nanolithography in order to acquire a patterning resolution beyond the diffraction limit. Nanostructured metallic films have been widely employed in PL to generate SPs upon illumination. For example, perforated features[12–14] and concentric ring gratings[15,16] fabricated on metallic layers on the nanometer scale were able to either generate localized SPs (LSPs) or couple propagating SPs (PSPs) and LSPs to achieve a stronger enhancement of resonant SPs. A 22-nm half-pitch resolution was attained by such a PL approach.[16] Unfortunately, to date, all the sub-diffraction-limit patterns experimentally acquired on photoresist by PL, including SL, exhibited a very poor contrast, corresponding to low profile depth. To be specific, the profile depth produced via SL is less than 10 nm[5–9] and only ~1 nm for PL,[16] which is far below the requirement of photolithography. In a photolithography context, contrast, i.e. the minimum visibility required for a resist pattern, is another fundamental requisition besides resolution and is required to be ≥1.5 for a negative resist (≥2.2 for a positive resist).[17] Improving contrast to suffice photolithography requirements has become a pressing task and its accomplishment would enable them to be ready for next-generation nano-patterning and fabrication.

The issue of loss is one of the fundamental challenges encountered by PL, as well as other metamaterials and plasmonic applications. Although Ag has been widely utilized in metamaterials and plasmonic nanodevices, benefiting from its low refractive index and low damping loss in the visible wavelength range,[18] its rough surface fabricated by conventional methods intrinsically leads to high loss. The influence of surface roughness of Ag films on the surface plasmons resonance

Dr. H. Liu, Dr. B. Wang, Dr. L. Ke, Dr. J. Deng, C. C. Choy, Dr. L. Shen, Dr. J. H. Teng
Institute of Materials Research and Engineering
Agency for Science
Technology and Research (A*STAR)
3 Research Link, Singapore 117602
E-mail: jh-teng@imre.a-star.edu.sg
Dr. M. S. Zhang
Data Storage Institute
Agency for Science
Technology and Research (A*STAR)
DSI Building, 5 Engineering Drive 1, Singapore 117608
Prof. S. A. Maier
Department of Physics
Imperial College London
London SW7 2AZ, UK
E-mail: s.maier@imperial.ac.uk

**DOI: 10.1002/adfm.201200788**

(SPR) and the optical properties on various Ag thin film structures have been actively studied.[19–21] To circumvent it, several novel methods have been developed, such as incorporating gain media for loss compensation[22] and creating ultrasmooth Ag films with sub-nanometer scale roughness to reduce scattering loss.[23–25] It was observed that both thin seed layers of nickel (Ni) and germanium (Ge) deposited via electron beam evaporation were competent to reduce the roughness of Ag films to around or even less than 1 nm.[19,24] In addition, a thin film of 50 nm Ag/2 nm Ni exhibited a higher sensitivity than a 50 nm Ag film upon the characterization of SPR implemented at a wavelength of 632 nm.[19] In fact, a smooth silver superlens induced by the above-mentioned seed layer effect has experimentally demonstrated a high resolution of 30-nm half pitch.[9] Very recently, we have also experimentally demonstrated a high contrast (>3) and sub-50 nm half-pitch resolution lithography via a silver superlens, in which the roughness of Ag film deposited on a polymer spacer was controlled to about 1.6 nm.[26] It has been motivated to perform a viability study on the smooth Ag films engineered via the ultrathin seed layers of Ni and Ge to be applied in SL, in order to achieve not only super resolution, but also adequate contrast. Moreover, a quantitative study of the surface roughness effect will facilitate an insight into SL performance.

In this work, we study the roughness effect of silver induced by thin seed layers on the SL performance. 35 nm Ag, 35 nm Ag/1 nm Ni, and 35 nm Ag/1 nm Ge, have been evaporated on top of a dielectric spacer to serve as superlenses. Step-by-step characterizations on the critically-controlled interfacial roughness of spacer-lens-resist structures have been performed by atomic force microscopy (AFM). Subject to a conventional UV photolithography process at 365 nm, the performance of these three superlenses, i.e., Ag, Ag/Ni and Ag/Ge were compared via AFM mapping over respective resists in terms of resolution, contrast and pattern transfer fidelity. Numerical calculations have been carried out to elucidate the underlying physics.

## 2. Results and Discussion

### 2.1. Fabrication and Characterization Procedures

**Figure 1** depicts the four-step fabrication process for a superlens layer made of 35 nm Ag, 35 nm Ag/1 nm Ni, or 35 nm Ag/1 nm Ge. Initially, a 40-nm thick chromium thin film was deposited onto quartz substrates by electron beam evaporation. A one-dimensional grating array of 100-nm pitch and 45-nm spacing was patterned on a resist via electron beam lithography (EBL) in an area of $30 \times 30$ ($m^2$. Subject to an ion milling process, it was transferred into the Cr to create the UV mask, as depicted in Figure 1a. A dielectric layer of 20-nm-thickness was formed as a spacer between the mask and the superlens by a planarization process including multistep coatings and etchings and a following reflow step, shown in Figure 1b. After that, 35 nm Ag, 35 nm Ag/1 nm Ni and 35 nm Ag/1 nm Ge were electron-beam evaporated respectively over the spacer to serve as the superlens, see Figure 1c. Finally, Figure 1d depicts a negative tone photoresist of ~100-nm-thick spin-coated over the superlens and subjected to a conventional photolithography process by flood-exposure to the 365 nm I-line at an exposure dosage of 480 mJ/cm$^2$. A control sample was prepared by replacing the superlens layer with an equal-thickness (35 nm) spacer layer and subjected to the same process conditions. Ultimately, the sub-diffraction-limit information was recorded into the surface topographic profile on the resist layer. The surface morphology of the prepared samples was assessed through a multimode AFM in a tapping mode at ambient conditions. Additionally, thin film thickness measurements were carried out via variable angle spectroscopic ellipsometry with a Cauchy model. (The experiment on sample preparation is detailed in Experimental Section.)

### 2.2. Surface Roughness Characterization

The spacer layer was fabricated to provide a uniform distance between the mask and superlens. Its thickness has to be accurately controlled to retain a sufficiently high amplitude of the evanescent field to excite SPs upon reaching the superlens layer. Other than that, the spacer also served as a planarization layer to remove topographical modulations of the grating mask as much as possible, as well as providing a smooth surface

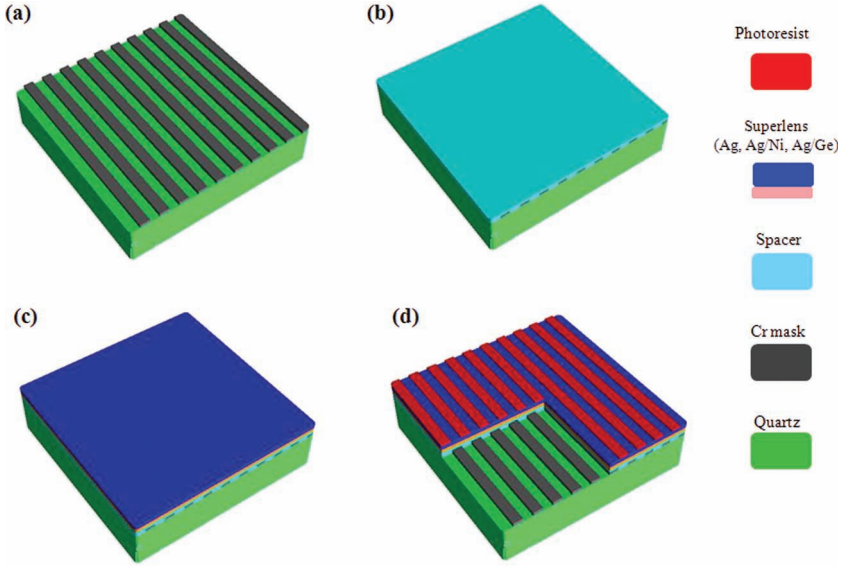


**Figure 1.** Schematics of the four-step fabrication process of sub-diffraction-limit lithography via 35 nm Ag, 35 nm Ag/1 nm Ni and 35 nm Ag/1 nm Ge superlenses. a) 100 nm-pitch 1D Cr gratings separated by a constant gap of 45 nm patterned by EBL and ion milling process. b) The Cr mask was planarized by a 20-nm thick mr-I T85 spacer. c) 35 nm Ag, 35 nm Ag/1 nm Ni and 35 nm Ag/1 nm Ge were evaporated as superlenses, respectively. In comparison, a control sample was prepared by replacing the Ag layer with an equal-thickness (35 nm) spacer layer. d) Subjected to a conventional UV photolithography process (365 nm wavelength), the sub-diffraction-limit resist patterns were recorded and characterized by AFM mapping.

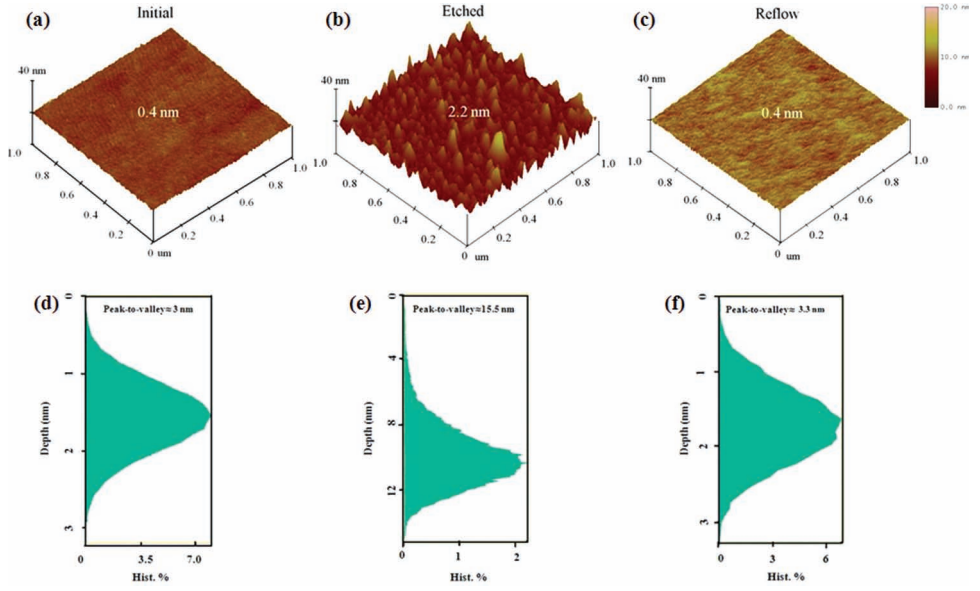


**Figure 2.** Surface morphological variations of the dielectric spacer during the planarization process from representative AFM images over an area of 1 μm × 1 μm The initial spacer layer of ~600-nm thickness by multi-step coating exhibited ~0.38 nm rms roughness. b) The surface became rough with ~2.2 nm roughness under oxygen plasma etching and the thickness was ~112.8 nm. c) After a reflow process, the ~20-nm thick spacer was smoothened significantly to ~0.4 nm roughness, almost equal to its original value. The 1 μm × 1 μm topographs (512 × 512 pixels) were automatically plane fitted with a color scale from 0 to 20 nm. d–f) Histograms of the surface-height data from the respective topographs. The peak-to-valley distances are (d) ~3 nm for the initial surface, (e) ~15.5 nm for the etched surface and (f) ~3.25 nm for the planarized surface, respectively.

to facilitate the deposition of the superlens layer. The surface roughness, in terms of root-mean-square (rms) roughness ($R_q$), and the peak-to-valley height difference were determined via AFM topography data followed by a quantitative and statistic surface analysis.

**Figure 2** shows surface roughness variations of the spacer layer throughout the planarization process. Initially, multistep spin-coating in conjunction with soft-baking were applied to achieve a semi-conformal coating of ~600-nm thickness with 0.4 nm roughness, as shown in Figure 2a. After that, oxygen plasma was used to etch down the thickness by multiple short-period cycles to stabilize the etching rate. Figure 2b shows that the surface became rough with a ~2.2 nm roughness, about 6 fold of its initial value, when the thickness was etched down to ~112.8 nm. Once a desirable thickness of ~20 nm was reached, the planarization process was completed with a reflow to smoothen the spacer surface. As shown in Figure 2c, the surface roughness was reduced to ~0.4 nm, similar to its initial value. Hence the planarization process effectively produced a spacer with a desired thickness value and a smooth surface. Panels d–f in Figure 2 are the corresponding histograms of surface-height data collected from the representative AFM images depicted in panels a–c. The histogram, which correlates to surface roughness, offers a quantitative measure of the maximum peak-to-valley distance and the average surface height deviation (SHD).[27] The spacer initially had a rather smooth surface with a peak-to-valley distance of only ~3 nm, corresponding to the smallest SHD as shown in Figure 2d. In contrast, it turned to be rough after subjecting to oxygen plasma etching with the highest peak-to-valley distance of ~15.5 nm, which was equivalent to the largest SHD shown in Figure 2e. Figure 2f depicts that the spacer exhibited a fairly smooth surface of a peak-to-valley distance of ~3.3 nm after planarization, which is, as well as SHD, comparable to its initial value.

**Figure 3** depicts the roughness of thin films of 35 nm Ag, 35 nm Ag/1 nm Ni and 35 nm Ag/1 nm Ge evaporated on top of the spacer. The roughness of these superlens layers measured in a 1 × 1 um$^2$ area are ~1.7 nm for Ag (Figure 3a), ~1.3 nm for Ag/Ni (Figure 3b) and ~1.2 nm for Ag/Ge (Figure 3c), respectively. The AFM results show that Ag deposited with a thin seed layer of Ge exhibits a superior smoothness to Ag/Ni followed by pure Ag but the maximum difference among them is only ~0.5 nm. The control sample exhibits the same smoothness as that shown in Figure 2a. Comparing to the previous report[24] in which the

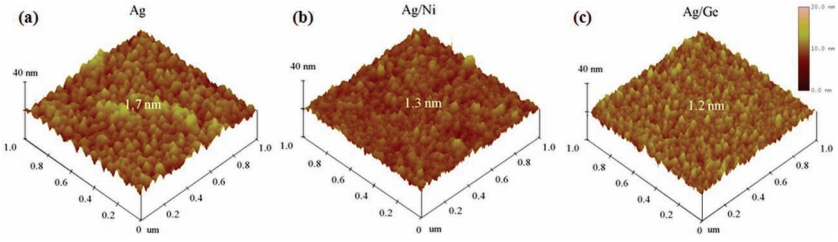


**Figure 3.** Surface morphologies of the Ag, Ag/Ni and Ag/Ge superlenses evaporated on top of spacer. The roughness measured by AFM over a 1 μm × 1 μm area are (a) 1.69 nm for Ag, (b) 1.34 nm for Ag/Ni and (c) 1.22 nm for Ag/Ge, respectively. A control sample exhibits the same smoothness as that shown in Figure 2a. (The color scale is from 0 to 20 nm).

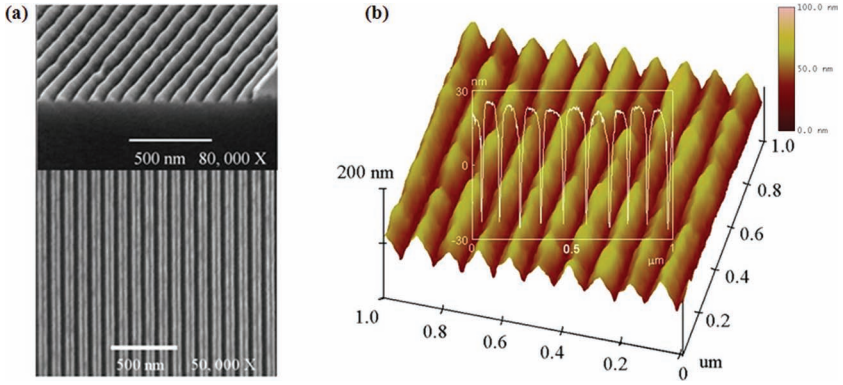


**Figure 4.** Surface characterizations of the 1D Cr mask. a) SEM picture of 100-nm pitch Cr gratings (inset: the cross sectional image was taken at 80° tilt angle). b) 3D contour of the topographic profile (1 μm × 1 μm) of the Cr grating mask, the inset shows its cross-sectional profile. (The color scale is from 0 to 100 nm).

Ag films were deposited with Ni and Ge seed layer on silicon and quartz substrates, the roughness tendency is identical. It shows that indeed a polymer substrate is able to facilitate a smooth deposition of Ag. A detailed study on the surface roughness of Ag films deposited on polymer was reported elsewhere.[25]

### 2.3. Resolution and Contrast

Surface characterizations of the 100-nm pitch Cr grating mask are depicted in **Figure 4**. Figure 4a is a scanning electron microscopy (SEM) image of the 1D Cr grating with 55-nm width and 45-nm gap. Its cross sectional picture taken at 80° tilt angle depicted in the inset clearly shows a complete etching without any residual Cr layer left in the valley in an ion milling process to form the mask. Figure 4b is the close-up AFM image (1 × 1 $\mu m^2$) with its cross-sectional contour plotted in the inset. An average profile depth of ~40 nm has been measured, which is equal to the targeted Cr film thickness by electron-beam evaporation. The Fourier spectrum analysis indicates that the Cr grating pattern period is about 100 nm.

**Figure 5** shows AFM images (3 × 3 $\mu m^2$) of the topographic characterization results of the attained resist patterns after the SL step via a Ag, Ag/Ni and Ag/Ge superlens respectively. Results from a control sample are also shown, and the insets represent corresponding cross sectional contours. Generally, all the resist patterns exhibit deep profiles, corresponding to high contrasts. The resist pattern after Ag SL (Figure 5a) has a fairly deep profile of ~45 nm, followed by ~30 nm for Ag/Ni (Figure 5b) and ~19 nm for Ag/Ge (Figure 5c). Above 5-fold improvement in terms of profile depth has been achieved even comparing to the best reported SL result,[5] In contrast, the AFM result of a control experiment plotted in Figure 5d shows that the Cr mask has been barely resolved with an extremely poor contrast of the resist profile. It indicates that sub-diffraction-limit patterning would not be attainable without a superlens to transmit and enhance evanescent waves.

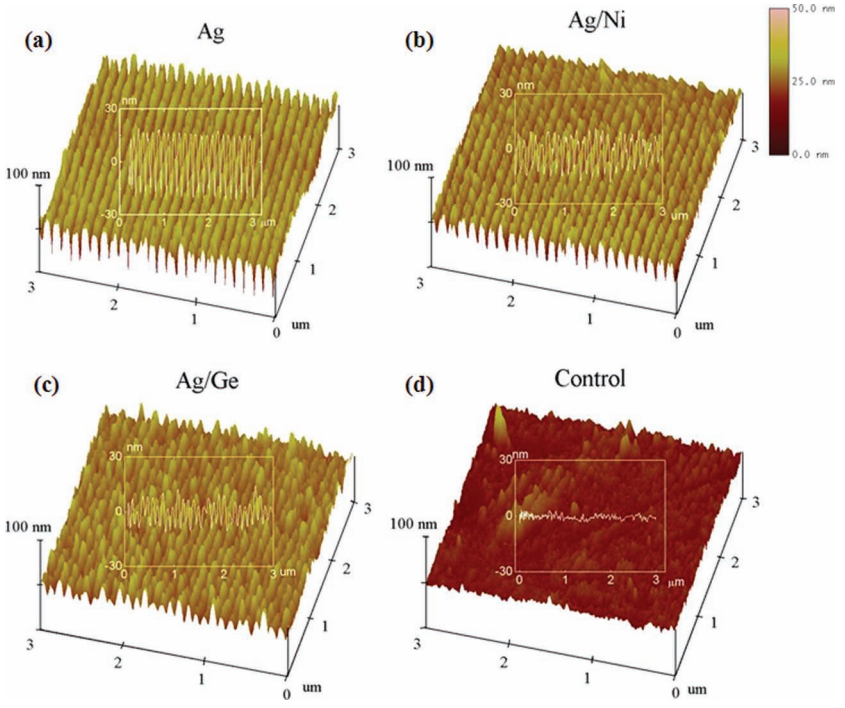


**Figure 5.** Topographic characterization of the resist patterns via superlenses. AFM images (3 μm × 3 μm) of the resist topographies acquired on a superlens of (a) Ag, (b) Ag/Ni, (c) Ag/Ge an (d) control sample. Insets show their corresponding cross sectional profiles. (The color scale is from 0 to 50 nm).

In near-field optical photolithography, upon illumination, the photoresist absorbs UV light energy to undergo a chemical change. The energy intensity is considered as a Gaussian distribution function with an exponential decay. The exposure profile of photoresist is under this model determined to be identical to that of the field energy density penetrating into the resist.[28] Since in SL the enhanced evanescent field is applied to the resist, the resolution ($R$) can then be defined by the full width at half maximum (FWHM) of its resulting exposure profile.[29] For the case of SL on a negative tone resist, the FWHM of the resist contour is equivalent to the edge-to-edge distance between adjacent gratings in the mask. Furthermore, the lithography contrast is directly related to the intensity contrast, which can be defined as $\gamma = I_{max}/I_{min}$, where $I_{max}$ equals to the maximum thickness of the exposed resist while $I_{min}$ is the minimum. In a Gaussian distribution profile, the deeper the contour, the higher the contrast, corresponding to a sharper optical image over resist. Therefore, two key performance indicators of SL, i.e. resolution and contrast, are measurable in a straightforward way by AFM mapping and topography analysis.

**Figure 6**a plots the normalized experimental surface contours of two adjacent gratings and corresponding resist profiles of various superlenses, which were collected from the respective AFM results. The resist profile of the Ag-only superlens exhibits a very high contrast of ~2.2 with a depth of ~45-nm while Ag/Ni has a moderate contrast of ~1.6 with a ~30-nm depth. By comparison, the surface contour of Ag/Ge presents a relatively low contrast of ~1.3 due to a depth of only ~19 nm. Referring to the minimum requirement of lithography contrast on a negative resist,[17] it verifies that the Ag superlens is capable of producing a high contrast resist pattern well above that criterion followed by Ag/Ni exhibiting a qualified value too. Taking the FWHM of ~45 nm for the Cr grating contour curve as a reference for the evaluation of the superlens resolution, the resist pattern in the Ag SL has a FWHM of ~76 nm. However, the inadequate contrast upon a relatively low profile depth of Ag/Ni and Ag/Ge makes it difficult to directly obtain its FWHM, as shown in Figure 6a. To facilitate the comparison, it is approximated to be the half width of the curve at half of the maximum intensity (0.5). Hence, the resolution of Ag/Ni is estimated to be ~91 nm while Ag/Ge demonstrates the poorest value of ~100 nm. In addition, pattern transfer fidelity, a ratio of FWHM between the Cr grating and resist pattern, respectively, is another factor for SL evaluation. The Ag superlens exhibits the best pattern transfer ability with a high fidelity ratio of ~0.6, while Ag/Ni comes next with ~0.5 followed by Ag/Ge of ~0.45. Hence it is apparent that all these three superlenses with well-controlled interfacial roughness are able to resolve and regenerate the sub-diffraction-limited Cr mask pattern into the resist pattern, but with distinct patterning qualities in terms of resolution, contrast and fidelity. Nevertheless, the smooth Ag superlens displays an exceptional lithography ability, mainly due to its low loss characteristic. In spite of a roughness improvement of about 0.4 nm, Ag/Ni demonstrates the second patterning quality as Ni is considerably absorptive in UV regime. In comparison, germanium, due to significant absorption in the UV regime, suffers from a very serious damping loss. The order of pitch size of the resist patterns is: Ag (101.9 nm), Ag/Ni (102.7 nm) and Ag/Ge (103.9 nm) based on the AFM results. The material loss is accountable for the tiny increment (<4%) of pitch size, which is almost negligible compared to the 100-nm pitch of Cr mask. The damping effect surpasses the surface roughness effect in determining the resolution and contrast when the superlens roughness is reduced to less than ~2 nm. Hence one should be cautious in using noble metals for which a thin adhesion layer is usually required. We can summarize that a superlens is capable for nanophotolithography with sufficient contrast and profile depth, if rigorous control on interfacial roughness to reduce the scattering loss is applied. **Table 1** lists the key specifications of SL achieved from our experiments and simulations.

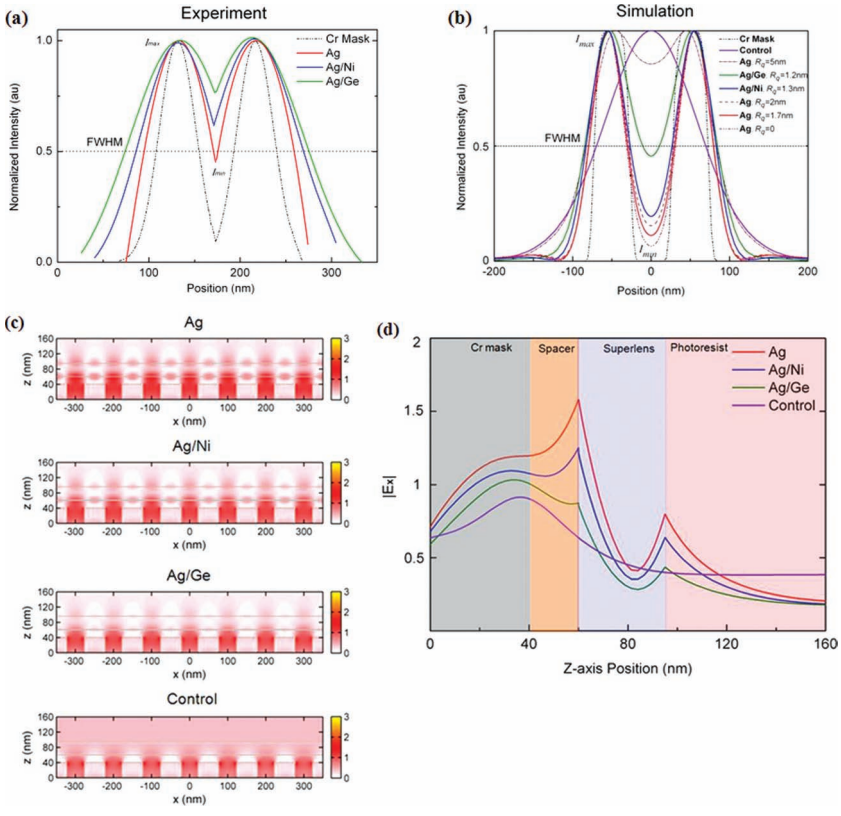


**Figure 6.** Analysis and simulation of sub-diffraction-limit and high contrast superlens lithography. a) Normalized experimental surface contours of mask and resist patterns via various superlenses. b) Computed pattern profiles of various superlenses taking into consideration of roughness ($R_q$) together with a perfect smooth Ag superlens. The mask and control pattern are also plotted. c) The amplitude distribution of electric field ($|E_x|$) along the longitudinal direction. d) The amplitude variation of electric field ($|E_x|$) penetrating the mask-lens-resist system.

**Table 1.** Key specifications of superlens lithography achieved by experiment and simulation.

| Superlens | Experiment | | | | | Simulation | | |
|---|---|---|---|---|---|---|---|---|
| | Surface Roughness, $R_q$ (nm) | Resolution/ FWHM (nm) | Contrast ($\gamma$) | Profile depth (nm) | Pattern transfer fidelity | Surface Roughness, $R_q$ (nm) | Resolution/ FWHM (nm) | Contrast ($\gamma$) |
| Ag | 1.7 | 76 | 2.2 | 45 | 0.6 | – | 49.8 | 9 |
| Ag/Ni | 1.3 | ~91 | 1.6 | 30 | 0.5 | – | 56 | 5.1 |
| Ag/Ge | 1.2 | ~100 | 1.3 | 19 | 0.45 | – | 73.7 | 2.2 |
| Ag | – | – | – | – | – | 0 | 48.5 | 15.2 |
| Ag | – | – | – | – | – | 2 | 50 | 6.5 |
| Ag | – | – | – | – | – | 5 | 166 | 1.2 |

To qualitatively investigate the roughness effect on patterning quality of a near-field SL, a computational analysis has been conducted. A transfer matrix approach[30] has been applied to calculate the point spread function (PSF) of the mask-lens-resist system for a better understanding of the influence of roughness for a UV light exposure at 365 nm (TM polarization). **Table 2** lists the dielectric constants of the materials employed in the SL system, which are taken from the literature through interpolation. The computational intensity contrasts of Ag, Ag/Ni, Ag/Ge superlenses and the control sample taking surface roughness retrieved from respective AFM data into consideration have been plotted in Figure 6b. For comparison, a perfectly smooth Ag film of equal-thickness (35 nm) without roughness is also included. The Ag superlens shows a high contrast of ~9 in combination of a FWHM of ~49.8 nm followed by Ag/Ni with a moderate contrast of ~5.1 and a slightly worse FWHM of ~56 nm, while Ag/Ge presents the lowest contrast of 2.2 in correlation with the worst FWHM of ~73.7 nm. The tendency of both resolution and contrast of various superlenses in the simulation follows the same order as that in experiment. The finer resolution and higher contrast values from the simulation can be ascribed to the neglect of fabrication imperfections and absorbance of the spacer layer. It is not surprising that a perfect Ag superlens of roughness-free exhibits the highest resolution of ~48.5 nm and contrast of ~15.2. The analytical results also indicate that the contrast would be remarkably degraded to only about 1.2 with a poor resolution of ~166 nm if the Ag roughness would exceed 5 nm, while sub-50 nm resolution with a corresponding high contrast (>6.5) is theoretically achievable by Ag superlens with roughness of less than 2 nm. In conjunction with the experimental results, the computational results substantiate that roughness is a critical factor determining the SL patterning quality.

**Table 2.** The dielectric constant ($\varepsilon$) of materials at 365 nm wavelength employed in the simulation of various superlenses.

| Materials | Cr[18] | Spacer[31] | Ag[18] | Ni[18] | Ge[18] | Resist[31] |
|---|---|---|---|---|---|---|
| Dielectric constant | −8.55 + 8.96i | 2.415 | −2.5667 + 0.599i | −2.0924 + 7.0347i | 10.7111 + 21.2408i | 2.719 |

### 2.4. Electric Field Distribution

Obtained using the finite-difference time-domain (FDTD) method, the panels of Figure 6c compare the amplitude distribution of the electric field ($|E_x|$) along the mask opening area in the longitudinal direction. The field distributions demonstrate that field amplitude and contrast enhancement follow the order of Ag, Ag/Ni, and Ag/Ge. Figure 6d plots the amplitude variation of the electric field component ($|E_x|$) penetrating into the SL system, from mask to spacer, lens and resist, for a quantitative comparison of the pattern transfer ability of various superlens systems. At the spacer-lens interface, the largest $|E_x|$ amplitude enhancement of ~1.6 is observed for Ag and ~1.3 for Ag/Ni. The mechanism of such an enhancement is attributed to the higher SPs excitation efficiency due to permittivity matching between Ag and spacer. The higher damping loss of germanium leads to a degradation of field enhancement, i.e. ~0.9 for Ag/Ge. Subsequently, the evanescent field passes through the superlens layer and gets enhanced at the lens-resist interface for all cases. The field amplitude enhancement is ~0.8 for Ag, ~0.6 for Ag/Ni and ~0.4 for Ag/Ge.

## 3. Conclusion

In summary, we have performed both experimental and computational studies on near field optical photolithography at a wavelength of 365 nm via Ag, Ag/Ni and Ag/Ge superlenses. The lithographic performances of these three superlenses are compared in terms of resolution, contrast and fidelity. With a critical step-by-step control of interfacial roughness to below ~2 nm in order to suppress scattering loss, all the superlens systems are able to produce sub-50 nm resolution patterns from a Cr mask. Among them, Ag exhibits the highest patterning performance followed by Ag/Ni and Ag/Ge. Both the experimental and analytical results substantiate that smooth interfaces are an essential factor to achieve high contrast and high fidelity lithography with sub-diffraction-limit resolution. Although ultrathin seed layers are able to reduce interfacial roughness, they are not necessary and in fact detrimental for superlens applications, due to the extra damping loss introduced. High contrast and super-resolution SL engineered through refining interfacial roughness provides a promising

route for high throughput and low cost nano-photolithography applications for the semiconductor and data storage industries.

## 4. Experimental Section

Initially, 40-nm thick chromium (Cr) was deposited onto quartz wafers (UV grade, 15 mm (L) × 15 mm (W) × 0.4 mm (H)) with a refractive index of 1.46 by electron beam evaporation (Denton Vacuum, Explorer) at room temperature. Electron-beam lithography (EBL) (ELS-7000, Elionix) was utilized to pattern the Cr mask. ZEP-520A resist was mixed with anisole at 1:1 ratio followed by spin-coating at 5000 rpm then soft-baking at 180 °C for 2 minutes on a hotplate. The EBL was performed with an exposure dosage of 240 μC/cm$^2$, beam current of 50 pA and acceleration voltage of 100 KV followed by development in o-Xylene for 30 seconds. An ion milling process (Nanoquest, Intlvac) was applied to transfer the resist patterns to the Cr mask under conditions of beam voltage/current of 300 V/110 mA, acceleration voltage/current of 100 V/ 6 mA, power of 180 W, chamber pressure of $2.54 \times 10^{-4}$ Torr and period of 6 minutes. Then, the residual resist was removed by soaking in Microposit remover 1165 (Shipley) for about 12 hours followed by oxygen plasma etching (Oxford RIE) under a power of 100 W and $O_2$ flow of 80 sccm for 2 minutes. By then, the 100 nm-pitch Cr grating had been created.

mr-I T85 (Micro Resist Technology, GmbH), a cyclic-olefin copolymer (COC), exhibiting excellent transmission and matching permittivity to Ag at 365 nm wavelength was chosen to serve as a spacer to planarize Cr mask. At first, multi-step spin coating cum soft-baking (about 6 steps) were applied to achieve a ~600-nm thick layer. In each step, the spin coating was done at about 3000 rpm for ~40 s followed by a soft baking at 140 °C for 2 minutes on a hotplate. Then, the spacer was thinned to a desirable thickness of ~20 nm by oxygen plasma etching (Sirus, Trion) under conditions of 20 W power, 20 sccm oxygen flow rate and 250 mTorr vacuum. Note that a single-step of continuous etching would increase the etching rate rapidly due to the raised chamber temperature. Therefore, multiple short-period cycles with 30 s etching at an interval of 30 s without breaking the vacuum were applied to acquire a constant etching rate of ~0.7 nm/s. Once the 20-nm thickness was reached, a reflow process was performed by baking samples on a hotplate at 150 °C well above the glass transition temperature ($T_g$) of spacer (85 °C) for 30 minutes. The planarization process ended with an ultrasmooth spacer.

After that, 35 nm Ag, 35 nm Ag with seed layers of 1 nm Ni and 1 nm Ge were deposited over the spacer through electron-beam evaporation (Explorer, Denton Vacuum) to serve as superlens layers, respectively. The evaporation rate for Ag was ~3 nm/s and ~0.2 nm/s for Ni and Ge. A negative tone photoresist of mr-UVL 6000 (Micro Resist Technology, GmbH) was spin-coated over those three superlenses at 3000 rpm to produce a ~100-nm thick patterning medium followed by soft-baking at 115 °C for 3 minutes. The samples then underwent I-line (365 nm wavelength) flood-exposure through a mask aligner (MA8/MA6, Karl Suss) with an exposure dosage of 480 mJ/cm$^2$ from the quartz substrate side followed by development in mr-Dev 600 (Micro Resist Technology, GmbH) for 50s and rinsed by IPA. In comparison, a control sample was prepared by replacing the superlens layer with an equally-thick (35 nm) spacer and subjected to the same conditions. Ultimately, the 1D sub-diffraction-limit patterns were recorded into the topographical profile of photoresist and characterized by AFM mapping.

All the thickness measurements were conducted using variable angle spectroscopic ellipsometry (WVASE32, J. A. Woollam), while surface morphology was assessed via a multimode AFM (Bruker) in a tapping mode at a scan rate of about 0.5 Hz. An ultrahigh resolution Scanning Electron Microscope (ESM 9000, Elionix) was utilized to take the SEM pictures of Cr mask.

## Acknowledgements

The project was financially supported by Agency for Science, Technology and Research (A*STAR) under grant number 0921540099 and 0921450030, the UK Physical Science and Engineering research Council (EPSRC) and the Leverhulme Trust.

Received: March 21, 2012
Published online: May 23, 2012

[1] J. B. Pendry, *Phys. Rev. Lett.* **2000**, *85*, 3966.
[2] A. A. Houck, J. B. Brock, I. L. Chuang, *Phys. Rev. Lett.* **2003**, *90*, 137401.
[3] A. Grbic, G. V. Eleftheriades, *Phys. Rev. Lett.* **2004**, *92*, 117403.
[4] A. N. Lagarkov, V. N. Kissel, *Phys. Rev. Lett.* **2004**, *92*, 077401.
[5] N. Fang, H. Lee, C. Sun, X. Zhang, *Science* **2005**, *308*, 534.
[6] H. Lee, Y. Xiong, N. Fang, W. Srituravanich, S. Durant, M. Ambati, C. Sun, X. Zhang, *New J. Phys.* **2005**, *7*, 1.
[7] D. O. S. Melville, R. J. Blaikie, *Opt. Express* **2005**, *13*, 2127.
[8] C. Jeppesen, R. B. Nielsen, A. Boltasseva, S. Xiao, N. A. Mortensen, A. Kristensen, *Opt. Express* **2009**, *17*, 22543.
[9] P. Chaturvedi, W. Wu, V. J. Logeeswaran, Z. Yu, M. S. Islam, S. Y. Wang, R. S. Williams, N. Fang, *Appl. Phys. Lett.* **2010**, *96*, 043102.
[10] T. Taubner, D. Korobkin, Y. Urzhumov, G. Shvets, R. Hillenbrand, *Science* **2006**, *313*, 1595.
[11] X. Zhang, Z. W. Liu, *Nat. Mater.* **2008**, *7*, 435.
[12] W. Srituravanich, N. Fang, S. Durant, M. Ambati, C. Sun, X. Zhang, *J. Vac. Sci. Technol. B* **2004**, *22*, 3475.
[13] X. Luo, T. Ishihara, *Appl. Phys. Lett.* **2004**, *84*, 4780.
[14] W. Srituravanich, S. Durant, H. Lee, C. Sun, X. Zhang, *J. Vac. Sci. Technol. B* **2005**, *23*, 2636.
[15] W. Srituravanich, L. Pan, Y. Wang, C. Sun, D. B. Bogy, X. Zhang, *Nat. Nanotechnol.* **2008**, *3*, 733.
[16] L. Pan, Y. Park, Y. Xiong, E. U. Avila, Y. Wang, L. Zeng, S. Xiong, J. Rho, C. Sun, D. B. Bogy, X. Zhang, *Sci. Rep.* **2011**, *1*, 1.
[17] M. J. Madou, in *Fundamentals of Microfabrication*, 2nd ed., New York, CRC, **2002**, Chap. 1, 9.
[18] E. D. Palik, Ed. in *Handbook of Optical Constants of Solids*, New York, Academic Press, **1991**.
[19] H. Liu, B. Wang, E. S. P. Leong, P. Yang, Y. Zong, G. Si, J. H. Teng, S. A. Maier, *ACS Nano* **2010**, *4*, 3139.
[20] L. Ke, S. Lai, H. Liu, K. Pei, B. Wang, J. H. Teng, *ACS Appl. Mater. Interfaces* **2012**, *4*, 1247.
[21] E. S. P. Leong, Y. Liu, B. Wang, J. H. Teng, *ACS Appl. Mater. Interfaces* **2011**, *3*, 1148.
[22] S. Xiao, V. P. Drachev, A. V. Kildishev, X. Ni, U. K. Chettiar, H. K. Yuan, V. M. Shalaev, *Nature* **2010**, *466*, 735.
[23] P. Nagpal, N. C. Lindquist, S. H. Oh, D. J. Norris, *Science* **2009**, *325*, 594.
[24] V. J. Logeeswaran, P. K. Nobuhiko, M. S. Islam, W. Wu, P. Chaturvedi, N. Fang, S. Y. Wang, R. S. Williams, *Nano Lett.* **2009**, *9*, 178.
[25] W. Chen, M. D. Thoreson, S. Ishii, A. V. Kildishev, V. M. Shalaev, *Opt. Express* **2010**, *18*, 5124.
[26] H. Liu, B. Wang, L. Ke, J. Deng, C. C. Chum, S. L. Teo, L. Shen, S. A. Maier, J. H. Teng, *Nano Lett.* **2012**, *12*, 1549.
[27] M. Higo, K. Fujita, Y. Tanaka, M. Mitsushio, T. Yoshidome, *Appl. Surf. Sci.* **2006**, *252*, 5083.
[28] E. Lee, J. W. Hahn, *J. Appl. Phys.* **2008**, *103*, 083550.
[29] T. Hakkarainen, T. Setala, A. T. Friberg, *Appl. Phys. B.* **2010**, *101*, 731.
[30] T. Hakkarainen, T. Setala, A. T. Friberg, *J. Opt. Soc. Am. A* **2009**, *26*, 2226.
[31] Micro Resist Technology GmbH, in *mr-I T85-Thermoplastic Polymer for Nanoimprinting Lithography*. www.microresist.com, **2011**.